Materials and Design 155 (2018) 59–70

Contents lists available at ScienceDirect

Materials and Design

journal homepage: www.elsevier.com/locate/matdes

Modelling fatigue delamination growth in fibre-reinforced composites: Power-law equations or artificial neural networks?

Giuliano Allegri*

Bristol Composites Institute (ACCIS), University of Bristol, UK

HIGHLIGHTS

- Modelling fatigue-driven delamination requires cyclic and monotonic components of the square-rooted energy release rate.
- Self-similarity principles inform the functional expression of the equations describing fatigue-driven delamination.
- Single-hidden-layer neural networks adequately describe the effects of mode-mixity and stress-ratio on delamination growth.
- Extreme machine learning allows representing physical constraints for modelling fatigue delamination growth.

GRAPHICAL ABSTRACT

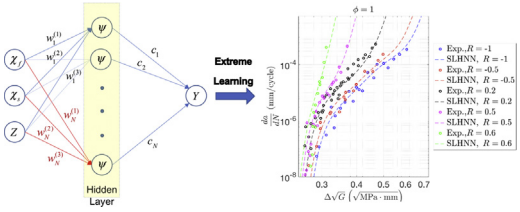

ARTICLE INFO

Article history:
Received 4 May 2018
Received in revised form 19 May 2018
Accepted 21 May 2018
Available online 26 May 2018

Keywords:
Delamination
Fatigue
Composites
Artificial neural networks

ABSTRACT

This paper discusses two alternative modelling approaches for describing fatigue delamination growth (FDG) in polymer-based fibre-reinforced composites, i.e. semi-empirical equations having a power-law form and artificial neural networks. Barenblatt's self-similarity principles are applied for identifying a suitable expression of the delamination driving force in terms of the square-rooted energy-release-rate range and the associated peak values. The general dependency of pre-factors and exponents of FDG power-laws on the stress-ratio and mode-mixity is discussed in detail. Single-hidden-layer neural networks (SHLNN) with the support of self-similarity principles are here proposed as an alternative to semi-empirical power laws for describing FDG in composites. A example application of SHLNN to mixed-mode and variable stress-ratio FDG is provided for the carbon/epoxy system T800H/#3631. The SHLNN predictions are compared to a semi-empirical fit based on a modified Hartman-Schijve power-law.

1. Introduction

The characterisation and modelling of fatigue delamination growth (FDG) have primary importance for the application of composites in a wide range of engineering sectors, e.g. aerospace, automotive, marine and wind energy. Nonetheless, the current design methodology for primary composites structures is still based on a "no-growth" approach for interlaminar cracks [41,48]. This entails sizing components for in-service strains that are limited to values well below the ultimate load carrying capability of fibre-reinforced composites. In aerospace applications, the maximum allowed strain for "no growth" is obtained from the compression after impact (CAI) strength of laminates and it is usually in the order of 4000 $\mu\epsilon$ at ultimate load [7,41,48].

* Room 2.34, Queen's Building, University Walk, BS8 1TR Bristol, UK.
E-mail address: giuliano.allegri@bristol.ac.uk.

https://doi.org/10.1016/j.matdes.2018.05.049
0264-1275/

Moving away from a "no growth" design philosophy can potentially yield a significant reduction of weight for composite structures, but this requires robust methods for FDG prediction in service.

Artificial neural networks (ANNs) have already been applied to the modelling of fatigue in composites. However, the relevant literature is entirely focussed on producing laminate-level SN curves via ANNs trained on representative subsets of experimental data.

Aymerich and Serra [6] employed a feed-forward ANN trained by back-propagation to predict the effect of the stacking sequence on the SN curve of prismatic AS4/PEEK coupons. These had been subject to tension-tension fatigue with stress ratio $R = 0.1$. The ANN-based methodology proved reasonably successful, albeit the authors recognised that a large training data set was required in order for the network to give an accurate representation of validation data. Nonetheless, the predictions of fatigue life were generally poor for stacking sequences that were not included in the ANN training data set. The authors pointed out that such a difficulty in "extrapolating" to scenarios beyond those considered in the ANN training was due to the multiple interacting and stacking-sequence dependent failure modes that govern the fatigue life, i.e. matrix cracking, delamination and final fibre failure.

Lee at al. [32] considered a set of 400 fatigue tests, which had been performed on 5 different composite materials, including carbon- and glass-reinforced plastics. The experimental database comprised tension-tension, as well as compression-compression tests, all performed on un-notched prismatic coupons. A feed-forward ANN with a single hidden layer was trained by back-propagation using a subset of the test data. The inputs to the network were the mechanical properties of the composites (i.e. tensile and compressive strengths and strains to failure; longitudinal Young's modulus), as well as the applied peak stress and the stress-ratio. The authors observed that the ANN was generally able to provide conservative estimates of the number of cycles to failure at any given stress level. However, all the coupons included in the experimental database had the same stacking sequence, i.e. $[(\pm 45, 0_2)_2]_S$. The authors also observed that it was not possible to predict the fatigue behaviour of carbon fibre-reinforced materials from an ANN trained via glass fibre composites data and vice versa.

El Kadi and Al-Yassaf [19] considered the application of feed-forward neural networks for modelling SN curves of unidirectional GFRP laminates with 0° and off-axis orientations. The dataset included both tension-tension fatigue and fully reversed loading cases. The authors investigated which input parameters would lead to the best predictions of experimental SN curves and concluded that those were the peak cyclic stress and the stress-ratio. They demonstrated that ANNs were able to represent the SN curve data with accuracy comparable to that of a Basquin type power-law that has the number of cycles to failure as argument.

This paper investigates the functional forms that a general FDG equation should take in order to respect Barenblatt's self-similarity principles. Such forms are discussed for the near-threshold case, the Paris regime and for cases where the peak energy release rate (ERR) approaches the material fracture toughness. A single-hidden-layer neural network (SHLNN), trained according to the extreme learning paradigm [25,26], is proposed as an alternative to power laws for modelling FDG.

This contribution is organised as follows: the concept of similitude via the normalisation of the variables governing FDG in composites is revisited in Sections 2.1 and 2.2. The application of self-similarity concepts to FDG is illustrated in Sections 2.3 and 2.4, whereby the approach employed by Barenblatt and Botvina [9,10] for cracks in alloys is extended to fatigue-driven delamination. The key assumption is that progressive interlaminar fracture occurs in a quasi-brittle fashion. Section 2.5 addresses the introduction of a characteristic length scale and a brittleness number to describe FDG in composites, based on the Mandell and Meier [33] non-singular crack-tip stress field. Section 3.1 summarises the principles of extreme machine learning for single-hidden-layer neural networks and the associated application to FDG via self-similarity principles. In Sections 3.2 and 3.3, FDG data published by Tanaka et al. [45-47] are considered as a case study, outlining the merits of a SHLNN approach compared to the usage of a power-law of the Hartman-Schijve type [13].

2. Similitude and self-similarity considerations for FDG

2.1. Delamination driving force

In a linear elastic fracture mechanics (LEFM) perspective, FDG is usually described using power-laws of the Paris type. Strictly speaking, a Paris-type equation should include the stress intensity factor (SIF) range ΔK as the crack driving "force" [24]. However, the most common modelling assumption for representing FDG is that the interlaminar growth rate depends either on the crack-tip ERR range ΔG or the peak ERR $G_{\max}$ [35]. In LEFM, all the aforementioned quantities are closely related and interchangable from a *mathematical* point of view. In particular, it is worth recalling that the maximum ERR values are related to the corresponding peak SIFs via [42,44]

$$G_{\mathrm{L,max}} = \alpha_{\mathrm{L}} K^2_{\mathrm{L,max}}, \tag{1}$$

where the subscript $\mathrm{L} = I, II$ denotes the fracture mode. The coefficients α_{L} have dimensions of compliance moduli and are recalled in Appendix A. For the relation between the SIF range and the corresponding peak value, one has

$$K_{\mathrm{L,max}} = \frac{\Delta K_{\mathrm{L}}}{1-R}, \tag{2}$$

where R is the stress ratio. Consequently, the expression of the ERR range via the peak SIF is

$$\Delta G_{\mathrm{L}} = \alpha_{\mathrm{L}} \left(1 - |R|R\right) K^2_{\mathrm{L,max}}, \tag{3}$$

which is valid for both positive and negative R ratios. Finally, the ERR and SIF ranges are related by

$$\Delta G_{\mathrm{L}} = \alpha_{\mathrm{L}} \frac{1-|R|R}{(1-R)^2} \Delta K^2_{\mathrm{L}}. \tag{4}$$

Many different semi-empirical equations have been proposed to describe FDG in laminated composites, aiming to find a power-law expression that can consistently represent the effect of stress-ratio and mode-mixity on the propagation of interlaminar cracks. Khan et al. [31] recently presented a comprehensive review of this topic. ERR-related expressions of the delamination driving force have been introduced in the literature because the modal components from Eqs. (3), and (4) can be summed in order to give a total peak ERR $G_{\max}$ (or a total ERR range ΔG) in mixed-mode fatigue scenarios. On the contrary, the SIFs are not additive. However, Rans et al. [37] pointed out that representing FDG data with respect to ΔG violates the *similitude* principle. This is because, given a delaminated specimen with a prescribed geometric configuration, the ranges of the interlaminar crack-tip SIFs ΔK_{L} are proportional to the range of the applied load $P_{\max} - P_{\min}$. On the other hand, the total ERR range ΔG is proportional to $P^2_{\max} - P^2_{\min} \neq (P_{\max} - P_{\min})^2$. This may actually cause a wrong interpretation of the effect of the stress-ratio, particularly in terms of the slope of the da/dN versus ΔG. For this reason, Rans et al. [37] proposed to consider the following revised definition of the ERR range:

$$\Delta^* G := \left(\sqrt{G_{\max}} - \sqrt{G_{\min}}\right)^2, \tag{5}$$

which correctly represents the variation of the applied load and therefore respects the similitude principle. The range of the square-rooted mixed-mode ERR $\Delta\sqrt{G}$ can be conveniently expressed as

$$\Delta\sqrt{G} := \sqrt{G_{\max}} - \sqrt{G_{\min}}. \tag{6}$$

Hence, Eqs. (5) and (6) imply that $\Delta\sqrt{G} = \sqrt{\Delta^* G}$.

2.2. Similitude parameters for FDG

Let the mixed-mode FDG in a unidirectional composite be considered, with a prescribed waveform of the cyclic load at a fixed frequency. The composite material is assumed to behave in a quasi-brittle fashion when it experiences interlaminar failure. Let us also restrict ourselves to the scenario where FDG takes place at constant temperature and where the moisture concentration within the material has a fixed uniform value. Given these hypotheses, the FDG rate can be expressed in very general terms as follows:

$$\frac{da}{dN} = f_0\left[\Delta\sqrt{G}, \sqrt{G_{\max}}, \Delta\sqrt{G}_{\text{th}}(\phi), \sqrt{G_C(\phi)}, \sigma_C(\phi), \ell_C(\phi), R, \phi, h, a\right], \tag{7}$$

where a is the delamination length and $\Delta\sqrt{G}_{\text{th}}(\phi)$ represents the mixed-mode dependent range of the square-rooted ERR at threshold, i.e.

$$\Delta\sqrt{G}_{\text{th}} = \left(\sqrt{G_{\max}} - \sqrt{G_{\min}}\right)_{\text{th}}. \tag{8}$$

Note that in general

$$\sqrt{G_{\max}} = \frac{\Delta\sqrt{G}}{1-R}. \tag{9}$$

In Eq. (7), ϕ is the mode-mixity, which is defined as

$$\phi := \frac{G_{II}}{G_I + G_{II}}. \tag{10}$$

G_C in Eq. (7) denotes the mixed-mode fracture toughness, while σ_C is the interlaminar strength of the composite material; finally, ℓ_C is length of the associated process zone ahead of the crack tip. The aforementioned three quantities are functions of the mode-mixity ϕ. Finally, h is the thickness of the cracked laminate. The latter is assumed to be much smaller than the laminate length and width and it can be therefore considered as the characteristic dimension of the elastic body.

Adopting length L and force F as fundamental units, the quantities that appear in Eq. (7) have the following dimensions:

$$\begin{aligned}
&[a] = [h] = [\ell_C] = [da/dN] = \mathrm{L},\\
&\left[\Delta\sqrt{G}\right] = \left[\sqrt{G_{\max}}\right] = \left[\Delta\sqrt{G}_{\text{th}}\right] = \left[\sqrt{G_C}\right] = \mathrm{F}^{1/2}\mathrm{L}^{-1/2},\\
&[\sigma_C] = \mathrm{F}\mathrm{L}^{-2},\\
&[R] = [\phi] = \mathrm{F}^0\mathrm{L}^0.
\end{aligned} \tag{11}$$

In analogy with the usual assumptions adopted for crack growth in alloys [9,18], let the characteristic length scale $\ell_C(\phi)$ and the square-rooted mixed-mode fracture toughness $\sqrt{G_C(\phi)}$ be considered as independent parameters. Therefore, invoking the Buckingham π theorem [14] allows rewriting Eq. (7) by considering only *seven* dimensionless numbers out of the *nine* initially introduced in Eq. (7), i.e.

$$\frac{1}{\ell_C}\frac{da}{dN} = f_1\left[\frac{\Delta\sqrt{G}}{\sqrt{G_C(\phi)}}, \frac{\sqrt{G_{\max}}}{\sqrt{G_C(\phi)}}, \frac{\Delta\sqrt{G}_{\text{th}}(\phi)}{\sqrt{G_C(\phi)}}, \frac{\sigma_C(\phi)\ell_C(\phi)}{G_C(\phi)}, \frac{h}{\ell_C(\phi)}, \frac{a}{\ell_C(\phi)}\right]. \tag{12}$$

At any given mode-mixity, the experimental evidence suggests that [24,46] 1) no crack growth occurs below the threshold square-rooted ERR range; 2) when the peak ERR reaches the material mixed-mode toughness, static fracture ensues. Hence, Eq. (12) can be recast in the following form:

$$\frac{da}{dN} = \ell_C(\phi) f_2\left[\chi_f, \chi_s, Z(\phi), \frac{h}{\ell_C(\phi)}, \frac{a}{\ell_C(\phi)}, R, \phi\right], \tag{13}$$

where the first three non-dimensional arguments are defined as

$$\begin{aligned}
\chi_f(\phi) &:= \frac{\Delta\sqrt{G} - \Delta\sqrt{G}_{\text{th}}(\phi)}{\sqrt{G_C(\phi)}},\\
\chi_s(\phi, R) &:= 1 - \frac{\sqrt{G_{\max}}}{\sqrt{G_C(\phi)}} = 1 - \frac{\Delta\sqrt{G}}{(1-R)\sqrt{G_C(\phi)}},\\
Z(\phi) &:= \frac{\sigma_C(\phi)\ell_C(\phi)}{G_C(\phi)}.
\end{aligned} \tag{14}$$

Since no FDG can occur below the fatigue threshold, we necessarily have $\chi_f \geq 0$. Similarly, FDG can take place only before static fracture, hence $\chi_s \geq 0$. For the function f_2 in Eq. (13), the following limits must hold: $f_2 \to 0^+$ for $\chi_f \to 0^+$, which corresponds to the threshold condition; and $f_2 \to \infty$ for $\chi_s \to 0^+$, the latter representing static fracture.

The parameter $Z(\phi)$ in Eq. (14) resembles the brittleness number introduced by Carpinteri [15] for describing the fracture of concrete beams. For a perfectly brittle material, there is no process zone ahead of the crack tip, hence $\ell_C(\phi) = 0$ and $Z(\phi) = 0$. However, in this case the derivations presented above are not valid, because the delamination length cannot be normalised via a null quantity. On the other hand, for quasi-brittle materials $\ell_C(\phi) \neq 0$, thus in general $Z(\phi) > 0$.

It is important to observe that establishing the similitude parameters for FDG via dimensional considerations does not provide any further information regarding the actual functional forms of either f_1 in Eq. (12) or f_2 in Eq. (13).

2.3. Self-similarity of FDG with respect to $\Delta\sqrt{G}$

Barenblatt [8-12] investigated the concept of self-similarity in continuum mechanics, with special emphasis on turbulence and fracture problems. Barenblatt's work was complemented and extended by Carpinteri [16], Spagnoli [43], Ritchie [39] and Ciavarella et al. [18], who examined the specific forms that fatigue crack propagation laws for alloys should take in order to comply with self-similarity principles. Generally speaking self-similarity implies that a physical phenomenon appears the same on multiple observation scales, both in time and space. However, provided that an arbitrary physical law is expressed via a set of fundamental non-dimensional "similitude" parameters, two different kinds of self-similarity are possible.

Self similarity of the *first kind* (also denoted as "complete") entails that, when one of the parameters tends either to zero or to infinity, there exists a corresponding *finite and non-zero* limit for the physical law. On the other hand, self-similarity of the *second kind* (or, equivalently, "incomplete") implies that the dependency of the physical law on one of the parameters can be suitably described via a power-law, which represents an "intermediate asymptote" [8,12]. In

the case where incomplete self-similarity holds with respect to a given parameter, the exponent of the associated power law cannot be obtained only by similitude considerations. Thus, the power-law exponent represents an inherent property of the phenomenon observed, which needs to be empirically assessed. Moreover, such an exponent depends on *all* the other non-dimensional numbers that appear in the equations governing the phenomenon considered [8,12,20]. Self-similarity of both kinds implies similitude, but not vice-versa.

Looking back at Eq. (13), it is here assumed that the laminate thickness h and the delamination length a are both much larger than the size of the process zone $\ell_C(\phi)$, i.e. $h/\ell_C \to \infty$ and $a/\ell_C \to \infty$. Invoking self-similarity of the first kind with respect to the aforementioned parameters, Eq. (13) becomes

$$\frac{da}{dN} = \ell_C(\phi) f_3\left[\chi_f(\phi), \chi_s(\phi,R), Z(\phi), R, \phi\right], \tag{15}$$

where $f_3 = \lim_{h/\ell_C\to\infty}\left(\lim_{a/\ell_C\to\infty} f_2\right)$. In other words, assuming complete self-similarity with respect to the ratio h/ℓ_C implies neglecting the size effect that would otherwise be present if the coupon thickness is comparable with the length of the process zone in a quasi-brittle material. Similarly, self-similarity of the first kind with respect to a/ℓ_C implies neglecting the effects associated with "mechanically" short cracks in quasi-brittle solids.

In Eq. (15) one has $\lim_{\chi_f\to 0} f_3 = 0$. Thus only self-similarity of the second kind can hold for f_3 with respect to its argument $\chi_f(\phi)$. As a consequence, Eq. (15) can be recast in the following power-law form:

$$\frac{da}{dN} = \ell_C(\phi)\chi_f^{\alpha\left[\chi_s(\phi,R),Z(\phi),R,\phi\right]} f_4\left[\chi_s(\phi,R), Z(\phi), R, \phi\right], \tag{16}$$

where $\alpha\left[\chi_s(\phi,R), Z(\phi), R, \phi\right] > 0$. Let us consider the scenario where the range of the square-rooted ERR is significantly larger than the corresponding threshold, i.e. $\Delta\sqrt{G}/\Delta\sqrt{G}_{\text{th}} \gg 1$, and the square-rooted peak ERR is much smaller than the associated mixed-mode toughness, i.e. $\sqrt{G_{\max}/G_C(\phi)} \ll 1$, which also implies $\chi_s \to 1$. Hence, Eq. (16) can be written as follows:

$$\frac{da}{dN} = C(R,\phi)\left(\Delta\sqrt{G}\right)^{\beta(R,\phi)}, \tag{17}$$

where

$$C(R,\phi) = \frac{\ell_C(\phi) f_4\left[1, Z(\phi), R, \phi\right]}{G_C^{\frac{1}{2}\beta(R,\phi)}(\phi)},$$
$$\beta(R,\phi) = \alpha\left[1, Z(\phi), R, \phi\right]. \tag{18}$$

Eq. (17) is an FDG equation of the classical Paris type, which is valid outside the near-threshold region. It is important to observe that, in analogy to what was concluded by Barenblatt and Bovina [9,10] for fatigue cracks in alloys, the pre-factor and the exponent of the Paris law for fatigue-driven delamination in composites are *not* material properties. In general, they also depend on the stress ratio and the mode-mixity. Eq. (17) confirms that, as pointed out by Rans et al. [37], $\Delta\sqrt{G}$ is the Paris-type crack driving force that respects the similitude principle. However, it must be also pointed out that, according to self-similarity principles, simply using $\Delta\sqrt{G}$ as crack driving force is not sufficient to explain the effects of the stress ratio and mode-mixity on FDG, because of the dependency of both C and β in Eq. (17) on R and ϕ.

A further important remark has to be made regarding the usage of the peak ERR $G_{\max}$ to describe FDG. Substituting Eq. (9) into Eq. (17) leads to the following equation:

$$\frac{da}{dN} = C^*(R,\phi)\left[\frac{G_{\max}}{G_C(\phi)}\right]^{\frac{1}{2}\beta(R,\phi)}, \tag{19}$$

where:

$$C^*(R,\phi) = \frac{\ell_C(\phi) f_4\left[1, Z(\phi), R, \phi\right]}{(1-R)^{\beta(R,\phi)}}. \tag{20}$$

Hence, describing FDG as a function of the peak ERR, with pre-factors and exponents that depend on the mode-mixity and stress-ratio, complies with self-similarity principles; hence, it does not violate similitude. Such an approach is therefore totally legitimate from both a mathematical and a physical point of view, provided that the ensuing ERR range is sufficiently far from the threshold region and that the peak ERR is much lower than the mixed-mode fracture toughness. FDG models have the functional form of Eq. (19) have been proposed by, among others, O'Brien et al. [35,36], Murri [34], Ratcliffe and Johnston [38], Andersons et al. [4] and Allegri et al. [1-3].

2.4. Self-similarity with respect to $\Delta\sqrt{G}$ and $\sqrt{G_{\max}}$

Let us consider the case where the range of the square-rooted ERR is of the same order of magnitude as the corresponding mixed-mode threshold and the peak ERR is not significantly smaller than the mixed-mode toughness. Under these assumption, the general expression of the FDG law is given again by Eq. (16). Actually, one may observe that the FDG rate diverges when $G_{\max} \to G_C$, i.e. $\lim_{\chi_s\to 0} f_4 = \infty$. Thus one may invoke incomplete self-similarity also with respect to χ_s and in this case Eq. (16) becomes

$$\frac{da}{dN} = \ell_C(\phi)\chi_f^{\gamma\left[Z(\phi),R,\phi\right]}\chi_s^{\delta\left[Z(\phi),R,\phi\right]} f_5\left[Z(\phi), R, \phi\right], \tag{21}$$

with $\gamma\left[Z(\phi),R,\phi\right] > 0$ and $\delta\left[Z(\phi),R,\phi\right] < 0$. Reverting to non-normalised variables, Eq. (21) can be rearranged as follows:

$$\frac{da}{dN} = F(R,\phi)\left(\Delta\sqrt{G} - \Delta\sqrt{G}_{\text{th}}\right)^{\alpha_1(R,\phi)}\left(1 - \sqrt{\frac{G_{\max}}{G_C(\phi)}}\right)^{\alpha_2(R,\phi)}, \tag{22}$$

where

$$F(R,\phi) = \frac{\ell_C(\phi) f_5\left[Z(\phi), R, \phi\right]}{G_C^{\frac{1}{2}\alpha_1(R,\phi)}(\phi)},$$
$$\alpha_1(R,\phi) = \gamma\left[Z(\phi),R,\phi\right], \quad \alpha_2(R,\phi) = \delta\left[Z(\phi),R,\phi\right]. \tag{23}$$

Assuming $\alpha_2 = -\alpha_1/2$, Eq. (23) gives the modified Hartman-Schijve [22,29] equation for FDG, which was proposed by Jones et al. [28] and recently revisited by Brunner et al. [13] and Yao et al. [49]. Considering $\alpha_2 = -\alpha_1$, Eq. (23) yields the FDG law that was introduced by Andersons et al. [5]. As in the case of equations of the Paris type, the pre-factor and exponents for phenomenological FDG models of the Hartman-Schijve class generally depend on the stress-ratio and mode-mixity. Therefore, postulating a relation between the exponents would represent a further restriction of the general form given in Eq. (22), which would need to be empirically justified.

Most importantly, for the class of FDG models represented by Eq. (22), the crack driving force comprises both a cyclic and a monotonic component. Hence, similitude does not hold when the load

range $P_{max} - P_{min}$ is kept constant, but the peak load P_{max} also plays a significant role in FDG.

When considering mode I fatigue crack propagation in alloys, typical threshold values for the SIF range are in the order of 4 MPa $\sqrt{m} \approx 160$ MPa $\sqrt{mm}$, while typical fracture toughness values are about 80 MPa $\sqrt{m} \approx 2500$ MPa $\sqrt{mm}$. Assuming a representative Young's modulus of the order of 100 GPa for alloys, the aforementioned values give a square-rooted ERR threshold and a toughness of $\Delta\sqrt{G_{th}} = 0.5\sqrt{\text{MPa mm}}$ and $\sqrt{G_C} = 8\sqrt{\text{MPa mm}}$, respectively. For a fibre reinforced composite, the experimental evidence [1, 2, 4, 24, 36, 45-47] suggests $\Delta\sqrt{G_{th}} = 0.3\sqrt{\text{MPa mm}}$ and $\sqrt{G_C} = 0.5\sqrt{\text{MPa mm}}$ for mode I; and $\Delta\sqrt{G_{th}} = 0.5\sqrt{\text{MPa mm}}$ and $\sqrt{G_C} = 1\sqrt{\text{MPa mm}}$ for mode II.

Hence, the Paris regime for fatigue crack growth in alloys, i.e. the $\Delta\sqrt{G}$ range in which the effect of $\sqrt{G_{max}}$ can be considered negligible, is significantly wider than the corresponding $\Delta\sqrt{G}$ domain for FDG in composites, for which in fact such a range may not exist at all, especially in mode I. This is also reflected by the fact that the β exponent for FGD in Eq. (17) takes values of about 10 for several CFRP materials [4,3,45,46,47], while the Paris law exponents in alloys are about 5. Overall, the argument outlined above supports the application of semi-empirical laws that have the form of Eq. (22) for describing FDG, as the Hartman-Schijve equation. Nonetheless, this implies dropping the load-only similitude argument and choosing a definition of the crack driving force that also involves the peak cyclic load via the peak ERR G_{max} or, equivalently, the square root of the latter.

2.5. Remarks on the brittleness number $Z(\phi)$ and the characteristic length $\ell_C(\phi)$

Mandell and Meier [33] proposed a non-singular crack tip stress field for describing the fracture process of cross-ply laminates comprising translaminar cracks. The Mandell and Meier stress field was applied to mode I and mode II fatigue-driven delamination by Andersons [4] and Allegri [3], respectively. The fundamental assumption introduced by Mandell and Meier is that for quasi-brittle materials there exists a region ahead of the crack tip where the stress is constant and progressive damage accumulation takes place, as shown in Fig. 1. Outside such a region, the asymptotic stress field has the classical $1/\sqrt{r}$ dependency, where r is the distance from the crack tip. For a mode I delamination, the Mandell and Meier stress field has the following expression:

$$\sigma_{33}(r) = \begin{cases} \sigma_C\sqrt{\frac{G_I}{G_{IC}}}, & r < \ell_{IC}, \\ \sqrt{\frac{G_I}{2\pi\alpha_I r}}, & r \geq \ell_{IC}, \end{cases} \tag{24}$$

where σ_{33} is the hoop stress and σ_C is the interlaminar tensile strength. From Eq. (24), one can immediately observe that when the ERR reaches the material fracture toughness, i.e. $G_I = G_{IC}$, then the value of the hoop stress for $r \leq \ell_{IC}$ equals the material strength, i.e. $\sigma_{33} = \sigma_C$. This way strength and fracture criteria are reconciled and made equivalent. The characteristic distance ℓ_{IC} corresponds to the location of the point ahead of the crack tip where the classical asymptotic stress field equals the material strength, i.e.

$$\ell_{IC} = \frac{G_{IC}}{2\pi\alpha_I\sigma_C^2}. \tag{25}$$

For mode II delamination, the expression of the Mandell and Meier shear stress field is formally analogous to that in Eq. (24), i.e.

$$\sigma_{13}(r) = \begin{cases} \tau_C\sqrt{\frac{G_{II}}{G_{IIC}}}, & r < \ell_{IIC}, \\ \sqrt{\frac{G_{II}}{2\pi\alpha_{II} r}}, & r \geq \ell_{IIC}, \end{cases} \tag{26}$$

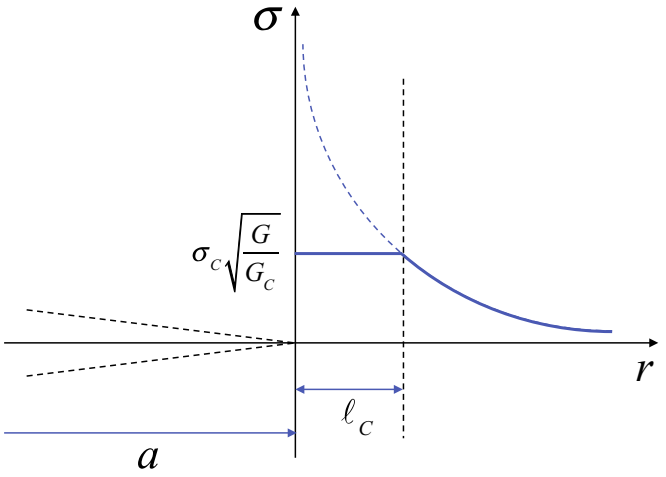

Fig. 1. Illustration of Mandell and Meier's crack-tip stress field [33,4,3].

where τ_C is the interlaminar shear strength. The characteristic distance in mode II is given by

$$\ell_{IIC} = \frac{G_{IIC}}{2\pi\alpha_{II}\tau_C^2}. \tag{27}$$

Similarly to the mode I case, from Eq. (26) one can observe that the shear stress σ_{13} reaches the corresponding material strength τ_C when $G_{II} = G_{IIC}$. From the considerations above, it is clear that ℓ_{IC} and ℓ_{IIC} represents the extent of the process zone in a Mandell-Meier quasi-brittle material, respectively for mode I and mode II. Considering the third of Eqs. (14), (25) and (27) yields the following expressions of the brittleness number $Z(\phi)$ for mode I and for mode II:

$$Z(0) = \frac{1}{2\pi\alpha_I\sigma_C}, \qquad Z(1) = \frac{1}{2\pi\alpha_{II}\tau_C}. \tag{28}$$

Eq. (28) shows that the brittleness number does not depend on the toughness, but it is related only to the stiffness and strength properties of the material. Regarding the application of the Mandell and Meier crack tip stress model to mixed-mode scenarios, let it be assumed that for $0 < \phi < 1$ Eqs. (24), and (26) still apply, but with an associated process zone length whose value $\ell_C(\phi)$ needs to be determined. For mixed-mode fracture, the linear ERR interaction criterion is here considered [27]:

$$\frac{G_I}{G_{IC}} + \frac{G_{II}}{G_{IIC}} = 1. \tag{29}$$

Observing that $G_I = (1-\phi)G$ and $G_{II} = \phi G$, the criterion in Eq. (29) is equivalent to state that fracture occurs when the total ERR $G = G_I + G_{II}$ reaches the mixed-mode fracture toughness:

$$G_C(\phi) = \frac{G_{IC}G_{IIC}}{G_{IC}\phi + G_{IIC}(1-\phi)}. \tag{30}$$

Moreover, in a mixed-mode case, Eqs. (24), and (26) yield

$$G_I = G_{IC}\left(\frac{\sigma_{33}}{\sigma_C}\right)^2, \quad G_{II} = G_{IIC}\left(\frac{\sigma_{13}}{\tau_C}\right)^2, \quad r < \ell_C(\phi). \tag{31}$$

Substituting Eq. (31) into the fracture propagation criterion Eq. (29) leads to

$$\left(\frac{\sigma_{33}}{\sigma_C}\right)^2 + \left(\frac{\sigma_{13}}{\tau_C}\right)^2 = 1, \tag{32}$$

which is the well-known stress-based quadratic criterion for delamination onset [27]. Hence, using the Mandell-Meier stress field, delamination initiation and propagation criteria can be made equivalent also in mixed-mode regimes. Substituting into Eq. (32) the values of the stresses at the boundary of the process zone, i.e. $r = \ell_C(\phi)$, and assuming $G_I + G_{II} = G_C(\phi)$ yield

$$\frac{1}{2\pi\ell_C(\phi)}\left(\frac{G_I}{\alpha_I\sigma_C^2} + \frac{G_{II}}{\alpha_{II}\tau_C^2}\right) = 1. \tag{33}$$

Eq. (33) leads to the following expression of the characteristic length in mixed-mode:

$$\ell_C(\phi) = \frac{G_C(\phi)}{2\pi}\left(\frac{1-\phi}{\alpha_I\sigma_C^2} + \frac{\phi}{\alpha_{II}\tau_C^2}\right). \tag{34}$$

Taking advantage of Eqs. (25) and (27), the mixed-mode characteristic length Eq. (34) can be equivalently expressed as

$$\ell_C(\phi) = \frac{\ell_{IC}(1-\phi)G_{IIC} + \ell_{IIC}\phi G_{IC}}{G_{IC}\phi + G_{IIC}(1-\phi)}. \tag{35}$$

From Eq. (35), it is straightforward to observe that $\ell_C(0) = \ell_{IC}$ and $\ell_C(1) = \ell_{IIC}$. Since within the process zone, i.e. for $r < \ell_C(\phi)$, the stresses are proportional to the square root of the ERR components, one may introduce an equivalent interlaminar stress $\bar{\sigma}$, which is related to the direct and shear traction components via the following identities:

$$\sigma_{33} = \bar{\sigma}\sqrt{1-\phi}, \quad \sigma_{13} = \bar{\sigma}\sqrt{\phi}. \tag{36}$$

Hence, delamination onset can be equivalently represented by the condition $\bar{\sigma} = \bar{\sigma}_C(\phi)$, where

$$\bar{\sigma}_C(\phi) = \frac{\sigma_C\tau_C}{\sqrt{\sigma_C^2\phi + \tau_C^2(1-\phi)}} \tag{37}$$

is a mode-mixity dependent strength. Combining Eqs. (30), (35) and (37), the following expression of the brittleness number $Z(\phi)$ is sought:

$$Z(\phi) = \frac{1}{2\pi\sqrt{\sigma_C^2\phi + \tau_C^2(1-\phi)}}\left[\frac{\tau_C(1-\phi)}{\alpha_I\sigma_C} + \frac{\sigma_C\phi}{\alpha_{II}\tau_C}\right]. \tag{38}$$

It is immediate to observe that Eq. (38) leads to Eq. (25) for $\phi = 0$ and to Eq. (27) for $\phi = 1$.

A final remark is due regarding the nature of the length scale $\ell_C(\phi)$, which has been obtained from quantities related to static fracture. There is no guarantee that the process zone length in fatigue will be equal to the one attained under static loading. However, it is reasonable to assume that the size of the process zone will be comparable in both cases. This is due to the fact that fractographic investigations showed that the failure morphology in delaminated composites is very similar under both quasi-static loading and fatigue [21].

3. SHLNN application to FDG

3.1. Modelling strategy

Extreme learning machines are feedforward single hidden-layer artificial neural networks (SHLNN) [25,26]. The training of this kind of networks is carried out by directly solving least-square problems and this provides a huge computational advantage compared to iterative learning schemes, such as back-propagation. SHLNN can be built using any arbitrary piecewise continuous function for the activation of the hidden neurons. The SHLNN weights for the hidden neurons can be randomly generated "a priori" from any continuous probability density function, i.e. the inner weights of the network can take fixed random values regardless of the dataset that the SHLNN is expected to learn. The training procedure affects only the weights associated with the output node, which is here considered to be simply additive. According to the universal approximation theorem, SHLNN can represent arbitrary continuous functions on any compact sub-domain of $\mathbb{R}^n$. Moreover, it is relatively straightforward to implement (semi-)monotonic constraints in the training procedure of SHLNN [50]. These constraints are key for representing existing knowledge regarding the physical phenomena that the network is assumed to learn.

In order to describe FDG via SHLNN, the delamination growth rate is here represented by the following variable:

$$Y(\phi) = \frac{2}{\pi}\tan^{-1}\left[\log_{10}\left(\frac{1}{\ell_C(\phi)}\frac{da}{dN}\right)\right]. \tag{39}$$

The introduction of the inverse tangent function and the $2/\pi$ normalisation factor in Eq. (39) allows mapping the FDG rates in the closed interval $[-1, 1]$. Albeit not strictly necessary from a theoretical point of view, rescaling the input and output variables is numerically beneficial for the training of ANNs [6,25].

The FDG-governing equation is postulated as

$$Y = g\left[\chi_f(\phi), \chi_s(\phi, R), Z(\phi)\right]. \tag{40}$$

Eq. (39) is a contracted form of Eq. (15), where the dependency of the FDG on the stress-ratio R is lumped into the "static" crack driving parameter χ_s. Similarly, the dependency on the mode-mixity ϕ is entirely ascribed to the brittleness number $Z(\phi)$ and the characteristic length $\ell_C(\phi)$. It is worth pointing out that Eq. (39) is valid only for cases where size effects can be discounted because of self-similarity of the first kind. As discussed in Section 2.3, this condition holds only for mechanically long cracks, i.e. $a \gg \ell_C(\phi)$, and micro-structurally "thick" laminates, i.e. $h \gg \ell_C(\phi)$.

A SHLNN representation of Eq. (39) comprising N hidden neurons can be given in the following form:

$$Y = \sum_{j=1}^{N} c_j\psi\left[w_j^{(1)}\chi_f + w_j^{(2)}\chi_s + w_j^{(3)}Z + \theta_j\right]. \tag{41}$$

In Eq. (41), $w_j^{(k)}$ with $k = 1, 2, 3$ are the random inner weights of the network, while θ_j are random activation thresholds for the SHLNN neurons; the c_j coefficients are the outer network weights, which have to be determined by training. Finally, ψ is the neuron activation function, which is here assumed to be sigmoidal [25], i.e.

$$\psi(z) = \frac{1}{1+e^{-z}}, \tag{42}$$

where $z \in \mathbb{R}$.

In extreme machine learning, the unknown outer weights c_j are determined by minimising the following cost function:

$$C := \sum_{k=1}^{M} \left\{ Y^{(k)} - Y\left[\chi_f^{(k)}, \chi_s^{(k)}, Z^{(k)}\right] \right\}^2, \tag{43}$$

where the index k in this context denotes the k-th experimental observation of FDG and M is the number of data points in the training set. Substituting Eq. (41) into the cost function given above yields

$$C = \sum_{k=1}^{M} \left\{ Y^{(k)} - \sum_{j=1}^{N} c_j \psi_j^{(k)} \right\}^2, \tag{44}$$

in which, for the sake of compactness

$$\psi_j^{(k)} := \psi\left[w_j^{(1)} \chi_f^{(k)} + w_j^{(2)} \chi_s^{(k)} + w_j^{(3)} Z^{(k)} + \theta_j \right]. \tag{45}$$

C from Eqs. (43), and (44) represents the quadratic norm of the error between the experimental FDG observations and the SHLNN output. Minimising C with respect to the outer weights

$$\frac{\partial C}{\partial c_l} = 0, \quad l = 1, \quad 2, \ldots, \quad N, \tag{46}$$

leads to the following linear system comprising N equations in N unknowns:

$$\sum_{j=1}^{N} \Psi_{lj} c_j = Q_l, \tag{47}$$

where

$$\Psi_{lj} := \sum_{k=1}^{M} \psi_l^{(k)} \psi_j^{(k)}, \qquad Q_l = \sum_{k=1}^{M} \psi_l^{(k)} Y_k. \tag{48}$$

Since the matrix Ψ_{lj} is symmetric, solving the linear system in Eq. (47) is equivalent to minimising the following quadratic form:

$$\mathcal{Q} = \frac{1}{2} \sum_{l=1}^{N} \sum_{j=1}^{N} c_l \Psi_{lj} c_j - \sum_{l=1}^{N} Q_l c_l. \tag{49}$$

From a physical point of view, the FDG rate is a non-decreasing function with respect to $\Delta\sqrt{G}$ for any given $\sqrt{G_{\max}}$. Moreover, the FDG is also non-decreasing as a function of $\sqrt{G_{\max}}$ for a prescribed $\Delta\sqrt{G}$. These semi-monotonic constraints hold independently of the mode-mixity considered. The aforementioned constraints can be enforced on the SHLNN representation by imposing

$$\begin{aligned} \tfrac{\partial Y}{\partial \chi_f} &= \sum_{j=1}^{N} c_j \psi' \left[w_j^{(1)} \chi_f + w_j^{(2)} \chi_s + w_j^{(3)} Z + \theta_j \right] w_j^{(1)} \geq 0, \\ \tfrac{\partial Y}{\partial \chi_s} &= \sum_{j=1}^{N} c_j \psi' \left[w_j^{(1)} \chi_f + w_j^{(2)} \chi_s + w_j^{(3)} Z + \theta_j \right] w_j^{(2)} \leq 0. \end{aligned} \tag{50}$$

Note that the sign of the second inequality in Eq. (50) is due to the fact that χ_s decreases with $\sqrt{G_{\max}}$ for any given $\Delta\sqrt{G}$. Eq. (50) represent the pre-existing physical knowledge of the FDG process that is embedded into the definition of the SHLNN. This is indeed a key difference between SHLNNs and multi-hidden-layer ANNs, since the latter do not allow a straightforward implementation of constraints in the form of Eq. (50). In this respect, a multi-hidden-layer ANN should be seen as a "black box", since its inherent structure neither provides any information about the phenomenon being represented, nor it allows defining physically-based (semi-)monotonicity constraints between inputs and outputs that hold independently from the training set considered.

It is worth observing that the derivative of the logistic function that appears in Eq. (50) is given by

$$\psi'(z) = \frac{e^{-z}}{(1 + e^{-z})}, \tag{51}$$

hence $\psi'(z) > 0, \ \forall z \in \mathbb{R}$. Therefore, the constraints in Eq. (50) can be equivalently expressed as follows:

$$\begin{aligned} \tfrac{\partial Y}{\partial \chi_f} &= \sum_{j=1}^{N} w_j^{(1)} c_j \geq 0, \\ \tfrac{\partial Y}{\partial \chi_s} &= \sum_{j=1}^{N} w_j^{(2)} c_j \leq 0. \end{aligned} \tag{52}$$

The minimisation of the quadratic form from Eq. (49) under the constraints in Eq. (52) represents a quadratic programming problem that can be easily solved using freely available numerical libraries.

3.2. FDG dataset

The FDG data generated by Tanaka et al. [45-47] for the carbon/epoxy system T800H/#3631 is considered as case study. This dataset comprises a full span of the mode-mixity range. Multiple stress-ratio values were considered in mode I and mode II, including fully-reversed loading in the latter case.

Tanaka et al. [45-47] also took special care in characterising the threshold values ΔK_{th} for the SIF range by identifying the regions of the da/dN versus ΔK diagram where the FDG rates deviated from a Paris power-law trend. A minimum of five experimental data points were obtained in those regions for the mixed-mode and mode II tests.

The stiffness and strength properties of T800H/#3631 are summarised in Table 1; the material has been considered transversely isotropic for the purpose of this analysis. The fatigue threshold and fracture toughness values for T800H/#3631 are given in Table 2. The mixed-mode fracture toughness values $G_C(\phi)$ have been calculated by means of Eq. (30) from the mode I and mode II data presented in Refs. [45] and [46]. In Table 2, the characteristic length $\ell_C(\phi)$ has been evaluated via Eq. (35), while the brittleness number $Z(\phi)$ has been calculated from Eq. (38). All the coupons tested (DCB for mode I; MMB for mixed-mode; ENF and ELS for mode II) were compliant with ASTM standards for *static* fracture toughness characterisations. The transversal geometric dimensions of the specimens were the same in all the tests (i.e. 6.2 mm thickness and 20 mm width). A Teflon insert film, 12 μm thick, was employed as a starter crack in all the coupons. The gauge length of the specimens was 100 mm, with starter cracks between 20 mm and 30 mm long.

Given these dimensions and the characteristic length values reported in Table 2, one can conclude that all the tests were carried out in a regime where the delaminations is "long" from a mechanical point of view, i.e. $a \gg \ell_C(\phi)$. However, it should also be observed that growing fatigue cracks directly from inserts may happen in a mechanically "short-crack" regime. This is due to the fact that the onset of a delamination from an artificial insert requires the formation of a process zone, so pre-cracking of the coupons should be undertaken before FDG data are collected. This pre-cracking should be carried out in fatigue and at the same mode-mixity of the actual FDG test to be performed, otherwise the geometry of the process

Table 1
Elastic properties of T800H/#3631.

E_1[a] (GPa)	E_3[a] (GPa)	G_{13}[a] (GPa)	ν_{13}[a]	σ_c[b] (MPa)	τ_c[b] (MPa)	[(c)]α_I (1/MPa)	[(c)]α_{II} (1/MPa)
137	8.1	4.8	0.31	69.6	102.9	9×10^{-5}	2.2×10^{-5}

[a] From Ref. [46].
[b] From Ref. [17].
[c] From Eq. (A.2).

zone would vary from the pre-cracking stage to the actual FDG characterisation. Attaining a "long" delamination regime, i.e. $a \gg \ell_C(\phi)$, is also crucial in order to ensure that LEFM can be correctly applied for the calculation of ERR-related quantities. If the size of the interlaminar crack is comparable with the characteristic length, the ERR should be estimated considering the actual cohesive nature of the delamination-tip stress field. Hence, employing the J-integral would be mandatory. In this respect, the $a \gg \ell_C(\phi)$ condition represents a regime that we can denote as "small-scale quasi-brittleness" (in analogy to the well-known "small-scale yielding" in alloys [39]), where LEFM holds.

Regarding the effect of the coupon thickness, the ratio $h/\ell_C(\phi)$ is not constant in the dataset, dropping from 67 in pure mode I (DCB coupons) to 8 in mode II (ENF coupons). The latter value may be too small for invoking self-similarity of the first kind with respect to the laminate thickness, but this should be verified performing additional fatigue tests on coupons with scaled dimensions, in order to assess the actual influence of the parameter $h/\ell_C(\phi)$. Such an investigation is beyond the scope of this paper, but it would be definitely worth undertaking for improving the understanding of FDG in composites.

The FDG data obtained in Refs. [45-47] are presented in Figs. 3–5. The dashed lines in the figure give the FDG rate obtained from the SHLNN, which will be discussed in detail in Section 3.3.

Concerning the experimental results, it is worth observing that the mode I FDG data presented in Fig. 3 are much sparser than those given in Figs. 4 and 5 for the mode II and mixed-mode cases, respectively. FDG thresholds are clearly visible in the latter two figures for propagation rates below 10^{-7} mm/cycle. More in detail, Fig. 4 shows that the mode II threshold expressed in terms of the square-rooted ERR does not depend on the stress ratio, since all the curves presented tend to converge to FDG rates below 10^{-7} mm/cycle, when $\Delta\sqrt{G}$ approaches the limit propagation value reported in Table 2. The mixed-mode data in Fig. 5 also suggest that $\Delta\sqrt{G}_{\text{th}}(\phi)$ steadily increases with the mode-mixity, i.e. delamination growth in the near threshold regime is delayed as the mode II fraction of the total ERR increases.

Regarding mode I, fitting two straight lines through the data in Fig. 3 for the $R = 0.2$ and $R = 0.5$ cases would suggest a decreasing FDG threshold for an increasing stress-ratio. This effect may depend on two different factors, namely fibre bridging and crack closure. Since the experiments in Refs. [45-47] were carried out in displacement control, the near threshold mode I data are obtained for a fully developed fibre-bridging zone that "shields" the crack tip [40]. This implies that the size of the bridged region should become smaller as the stress ratio increases, thus providing less shielding. Since the peak delamination opening displacement increases with the stress-ratio when $\Delta\sqrt{G}$ is kept constant, one may conclude that bridging fibres are more easily broken and/or pulled out as the stress-ratio is raised, thus reducing the shielding effect. Nonetheless, Khan et al. [30] conducted mode I FDG experiments whereby they progressively cut bridging fibres as the delamination advanced. Their results suggest that the effect of the bridging on the near-threshold FDG rates is very limited. Clearly, in DCB coupons fibre bridging become more and more prominent as the delamination advances, so the resulting driving force should be

Table 2
Fatigue thresholds and fracture toughness of T800H/#3631.

ϕ	$\Delta\sqrt{G}_{\text{th}}$[a] $\sqrt{\text{MPa mm}}$	G_C kJ/m^2	ℓ_C[c] (mm)	Z[d]
0	0.134	0.180[a]	0.066	25.3
0.42	0.206	0.268[b]	0.134	39.5
0.64	0.209	0.360[b]	0.205	49.1
0.84	0.236	0.523[b]	0.332	59.8
1	0.259	0.821[a]	0.563	70.5

[a] From Ref. [45-47].
[b] From Eq. (30).
[c] From Eq. (35).
[d] From Eq. (38).

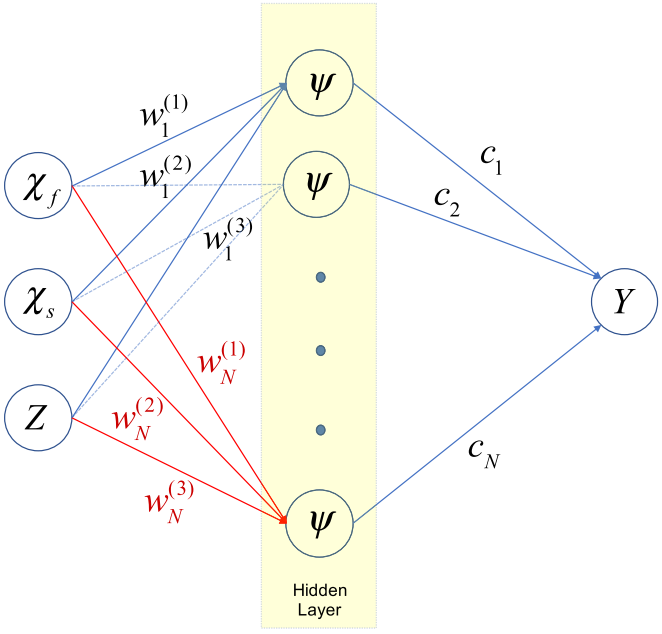

Fig. 2. Architecture of SHLNN for FDG description.

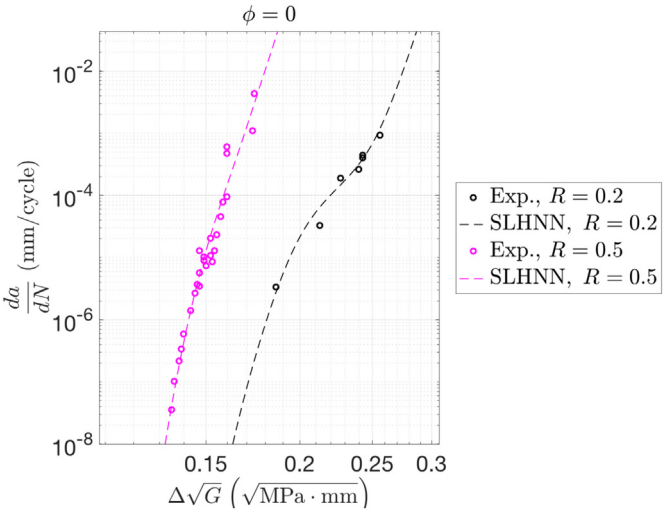

Fig. 3. Mode I FDG data for T800H/#3631 [45-47]; SHLNN output in dashed lines.

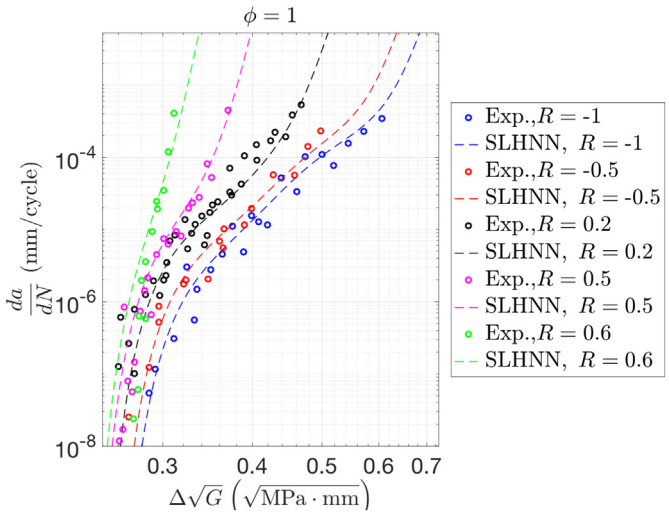

Fig. 4. Mode II FDG data for T800H/#3631 [45-47]; SHLNN output in dashed lines.

corrected in order to obtain "bridging-free" FDG rates [49]. Such a correction is not implemented in this paper, because it would require a static R-curve [34,38,49] for the material considered here, which unfortunately is not available. Regarding crack closure in delamination growth, Hojo et al. [23] observed that the effective SIF range in near threshold FDG is only marginally affected by the presence of closure. Khan et al. [30] recently came to the same conclusion. It seems therefore reasonable to assume that the $\Delta\sqrt{G_{\text{Ith}}}$ is independent from the stress-ratio.

It is also worth observing that, when $\Delta\sqrt{G}$ alone is considered as crack driving force, the FDG rates obtained at different stress-ratios do not collapse on the same curve for the material system considered here. $\sqrt{G_{\max}}$ also plays a significant role, as the FDG becomes significantly faster when the peak ERR increases. However, such an effect appears to be an inherent property of FDG in fibre-reinforced composites, rather than a consequence of "extrinsic" mechanisms [40], such as fibre bridging or interlaminar crack closure.

Finally, the scatter of experimental data in Figs. 3–5 is significant, yet representative of the typical level of uncertainty observed for FDG in composites. Yao et al. [49] demonstrated that the modified

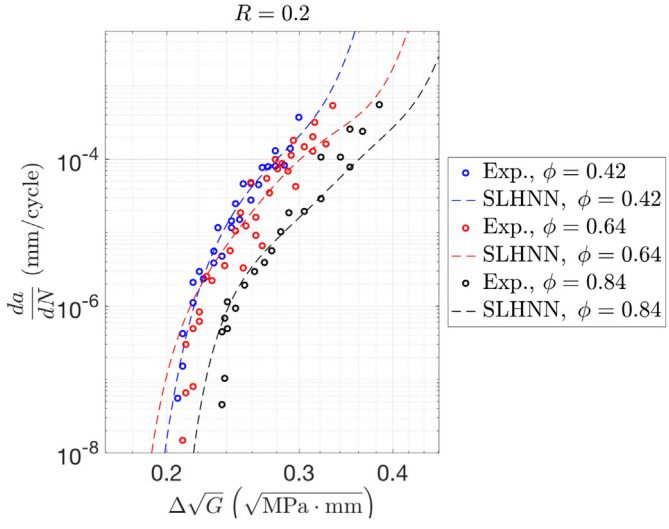

Fig. 5. Mixed-mode FDG data for T800H/#3631 [45-47]; SHLNN output in dashed lines.

Hartman-Schijve equation can be employed to generate an "A-basis" FDG rate for the robust design of composite structures. The SHLNN approach presented here aims to obtain average delamination propagation rates, but an extension of the neural-network model to the prediction of the FDG data scatter will be considered in future work.

3.3. Results and discussion

The training and validation of the SHLNN sketched in Fig. 2 were carried out by subdividing the results of the experimental FDG tests in two datasets, as illustrated in Table 3. The purpose of such subdivision was to provide a sufficient amount of information for the SHLNN to learn the effect of the stress-ratio and mode-mixity, considering extreme as well as intermediate values of both parameters as training scenarios. Overall, 60% of the experimental data were used for training the SHLNN, while 40% were employed for validation purposes. The input variables, i.e. χ_f, χ_s, Z were all linearly rescaled in order to range between −1 and 1.

The inner weight and threshold values in Eq. (41) were sampled according to a Gaussian distribution with zero mean and unit standard deviation. The outer weights c_j of the SHLNN were calculated by solving the quadratic programming problem involving the minimisation of Eq. (49) with the constraints Eq. (52); this was done employing the routine QUADPROG available in MATLAB 2017a, with the "interior-point" method as solution algorithm. The number of neurons in the hidden layer was progressively increased and the associated root mean square error (RMSE) with respect to the input dataset computed. The RMSE is related to the cost function from Eq. (44) via the relation $RMSE = \sqrt{C/M}$. A number of hidden neurons N ranging between 10 and 10^3 was considered; the resulting RMSE values with respect to the training dataset are plotted in Fig. 6. The plateauing of the RMSE as the number of neurons is increased can be easily appreciated. In order to avoid over-fitting phenomena, the trained SHLNN configuration considered here comprises 110 hidden neurons (red datum in Fig. 6), for which the RMSE is only 3% above the error value that would be attained for $N = 1000$. Moreover, a further simplification can be introduced by considering the "spectrum" of c_j values and dropping the outer weights that can be considered negligible according to the following criterion:

$$\frac{|c_j|}{\max(|c_j|)} \leq \delta, j = 1,\ 2, \ldots\ N, \tag{53}$$

where δ is a prescribed threshold. Assuming $\delta = 10^{-6}$ and $N = 110$, according to the criterion in Eq. (53), only 18 of the c_j weights need to

Table 3
Summary of training (T) and validation (V) cases for the SHLNN; the second and third rows for each mode-mixity value give the R^2 correlation coefficient for the SHLNN model and the Hartman-Schijve (HS) Eq. (54).

				R		
ϕ	Model	−1	−0.5	0.2	0.5	0.6
0		–	–	T	T	–
	SHLNN	–	–	0.970	0.939	–
	HS	–	–	0.987	0.881	–
0.42		–	–	T	–	–
	SHLNN	–	–	0.956	–	–
	HS	–	–	0.949	–	–
0.64		–	–	V	–	–
	SHLNN	–	–	0.890	–	–
	HS	–	–	0.879	–	–
0.84		–	–	V	–	–
	SHLNN	–	–	0.911	–	–
	HS	–	–	0.861	–	–
1		T	V	T	V	T
	SHLNN	0.948	0.959	0.783	0.864	0.713
	HS	0.955	0.955	0.802	0.800	0.918

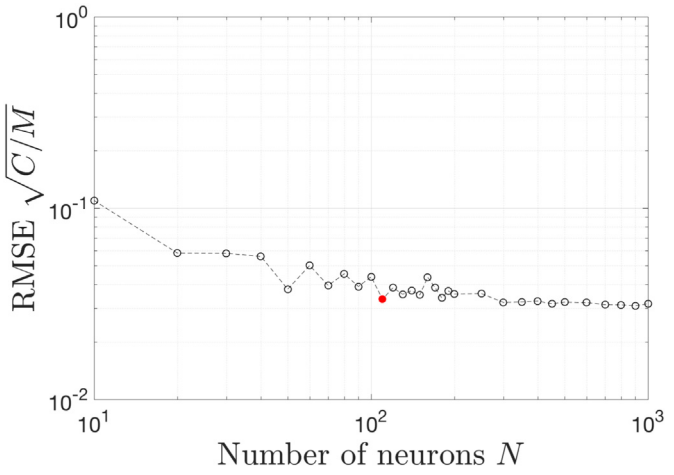

Fig. 6. RMSE of SHLNN calibration. The red circle indicates the hidden-layer size for the trained network, i.e. $N = 110$.

be retained. The increase of RMSE caused by pruning 92 of the neurons from the hidden layer is less than 0.1% when compared to the value attained for $N = 110$. Hence, the SHLNN expansion in Eq. (41) can be truncated to 18 terms without compromising the accuracy of the FDG representation.

It is also worth remarking that the solution of the quadratic programming problem for the determination of the outer weight c_j is extremely fast, requiring a maximum of 20 iterations of the interior-point algorithm even for $N = 1000$. The total training run-time is typically less than 5×10^{-2} s on a 2.8 GHz Intel Core-i7 PC with 8 Gb of RAM.

In order to compare the SHLNN approach with a more "traditional" phenomenological model based on a power law, the modified Hartman-Schijve (HS) equation proposed by Brunner et al. [13] and Yao et al. [49] is here considered:

$$\frac{da}{dN} = F(R,\phi)\left[\frac{\Delta\sqrt{G} - \Delta\sqrt{G}_{\text{th}}(\phi)}{\sqrt{1-\sqrt{G_{\max}}/G_C(\phi)}}\right]^{\alpha(R,\phi)} \tag{54}$$

As discussed in Section 2.4, the FDG propagation law in Eq. (54) is a particular case of the more general form given in Eq. (22). The pre-factor F and exponent α in Eq. (54) have been computed by fitting the experimental data from Tanaka et al. [45-47]. These fits require determining individual values of the pre-factor and the exponent for each combination of mode-mixity and stress-ratio, thus leading to 20 independent values of F and α for the 10 experimental cases in Table 3. On the other hand, the SHLNN model requires determining 18 outer weights. No attempt is made here to introduce specific mathematical expressions for the dependency of the pre-factor and the exponent on R and ϕ for the HS equation in Eq. (54). The purpose of this discussion is to demonstrate that the SHLNN model can predict with reasonable generality the effects of the stress-ratio and mode-mixity via the parameters χ_f and $Z(\phi)$.

The coefficients of determination R^2 (not to be confused with the square of the stress-ratio) for the SHLNN and HS models are presented in Table 3. These coefficients are calculated considering the $\log_{10}(da/dN)$ as output variable for both models. Generally speaking, the coefficients of determination obtained for the SHLNN fit are higher than those calculated for the HS model, suggesting an overall better performance of the neural network-based approach. This is true also for the validation cases that were not included in the training dataset, thus demonstrating that the SHLNN model can generalise trends. However, there are two significant exceptions to what has been just stated: namely, the HS equation outperforms the SHLNN model in mode II at the stress ratios $R = 0.2$ and $R = 0.6$. In both cases, as it can be appreciated in Fig. 4, the SHLNN prediction is conservative in the threshold regime, i.e. for FDG rates below 10^{-7} mm/cycle. This is due to the fact that, for $\Delta\sqrt{G}$ constant, the second of the constraints in Eq. (52) implies that the crack growth rate must be non-decreasing with respect to the stress-ratio R at any given mode-mixity. In order to understand this point, let us consider $\Delta\sqrt{G}$ constant and take advantage of the second of Eqs. (14) and (9); hence, the following identities can be derived from a straightforward application of the chain rule:

$$\frac{\partial Y}{\partial R} = \frac{\partial Y}{\partial \chi_s}\frac{\partial \chi_s}{\partial R} = -\frac{1}{\sqrt{G_c(\phi)}}\frac{\partial Y}{\partial \chi_s}\frac{\partial \sqrt{G_{\max}}}{\partial R} = \\ = -\frac{\Delta\sqrt{G}}{\sqrt{G_c(\phi)}}\frac{\partial Y}{\partial \chi_s}\frac{\partial}{\partial R}\frac{1}{1-R} = -\frac{\Delta\sqrt{G}}{\sqrt{G_c(\phi)}}\frac{\partial Y}{\partial \chi_s}\frac{1}{(1-R^2)} \geq 0, \tag{55}$$

where the last inequality holds by virtue of the second of Eq. (52). Hence, in the SHLNN output, individual FDG curves at the same mode-mixity and different stress ratios cannot overlap, albeit they will tend to converge as $\Delta\sqrt{G}$ approaches the threshold value. This is exactly the behaviour that can be seen in Fig. 4. However, the experimental curves for different stress ratios actually cross over in the near-threshold regime, most possibly due to the inherent errors associated with measuring very small FDG rates. This is true in particular for $R = 0.2$ and $R = 0.6$ in mode II, i.e. in the cases where, unsurprisingly, the SHLNN model achieves the lowest coefficients of determination.

Considering the data plots in Figs. 3–5, one can observe that the high coefficients of determination for the SHLNN model generally correspond to an excellent fit of the experimental FDG rates, for both training and validation cases. The largest deviation from the test results are observed in the threshold regions, where the SHLNN predictions tend to be conservative. The trained SHLNN also captures the divergence of the FDG rates when the peak energy release rate approaches the material fracture toughness.

Fig. 7 illustrates the dependency of the exponent α in the HS law as a function of the stress-ratio and the mode-mixity. It is important to observe that, in mode II, the exponent tends to increase with the stress-ratio when $R > 0$ and that there seems to be a minimum of α for $R \approx 0$. However, the exponent rises again when shear load reversal are present, i.e. with R becoming increasingly negative. Due to the limited amount of data available in mode I, no definitive conclusion can be drawn regarding the dependency of the FDG exponent α on R.

At the stress-ratio of $R = 0.2$, the HS exponent tends to decrease with the mode-mixity. This trend becomes much clearer when α is plotted as a function of the brittleness number $Z(\phi)$, as in Fig. 8. This is a further confirmation that the brittleness number is an important parameter for describing FDG in composites and it should be properly accounted for when introducing phenomenological models for progressive delamination growth.

The charts illustrating the HS power-law fit of the experimental FDG data are included in the Supplementary material provided with this paper, together with a table reporting the F and α parameters obtained from the regressions based on the HS equation.

4. Conclusions

Based on the theoretical analysis and numerical results presented in the paper, the following conclusions can be drawn:

1. The similitude of applied loads, which is underpinned by the usage of $\Delta\sqrt{G}$ as crack driving force, is not sufficient for explaining the effect of stress-ratio on FDG in fibre-reinforced

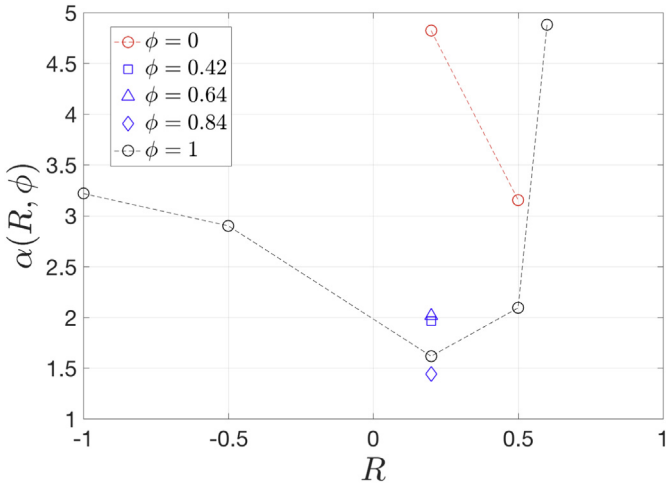

Fig. 7. Exponent of HS Eq. (54) as a function of stress-ratio R and mode-mixity ϕ.

composites. The peak energy release rate G_{max} attained in a fatigue cycle also plays a significant role. Considerations based on incomplete self-similarity suggest that, in line with the most recent literature, FDG in fibre-reinforced composites is better described using semi-empirical power-laws of the Hartman-Schijve type. This is because the Paris range for FDG in composites is relatively narrow, i.e. delamination thresholds are much closer to static fracture toughness values when compared to the corresponding characteristic properties of fatigue-driven cracks in alloys.

2. If FDG occurs in the Paris range, power-law models based either on $\Delta\sqrt{G}$ or on G_{max} are equivalent in a self-similarity (and hence similitude) perspective. However, self-similarity implies that the pre-factor and the exponent of the FDG power-law equations depend on the stress-ratio and mode-mixity. The brittleness number $Z(\phi)$ introduced in this paper for mixed-mode FDG helps explaining the latter dependency.
3. Two different kinds of size-effects may exist regarding FDG: the first is governed by the ratio of the delamination length a to the characteristic micro-structural length ℓ_C, which is representative of the scale of the crack-tip process zone in quasi-brittle materials. The second size effect depends on the ratio of the laminate thickness h to the micro-structural length scale ℓ_C. These effects can be discounted by virtue of self-similarity of the first kind, provided that the aforementioned ratios are both sufficiently large. However, such a condition may not necessarily hold, especially when FDG is characterised in mode II using relatively thin laminates.
4. SHLNNs offer a viable solution for describing FDG in composites. This paper has shown that a SHLNN comprising 18 hidden neurons with sigmoid activation function can be trained to represent FDG data with accuracy comparable, if not superior, to that obtained employing a recent modified version of the Hartman-Schijve equation. The network inputs have been determined based on the same self-similarity considerations recalled in point 1 above. The inputs are expressed via the toughness-normalised square-rooted ERR range $\Delta\sqrt{G}$ and peak ERR value G_{max}, as well as the brittleness number $Z(\phi)$. One of the key advantages of using SHLNN for representing FDG is that the network can be trained using an extreme learning approach, which also allows imposing (semi-)monotonic constraints on the network output as a function of the inputs. These constraints can effectively represent inherent features of the observed physical behaviour, e.g. the fact that FDG must be an increasing function of the square-rooted ERR range $\Delta\sqrt{G}$, thus removing one of the main limitations associated with the "black-box" nature of multi-hidden-layer ANN.

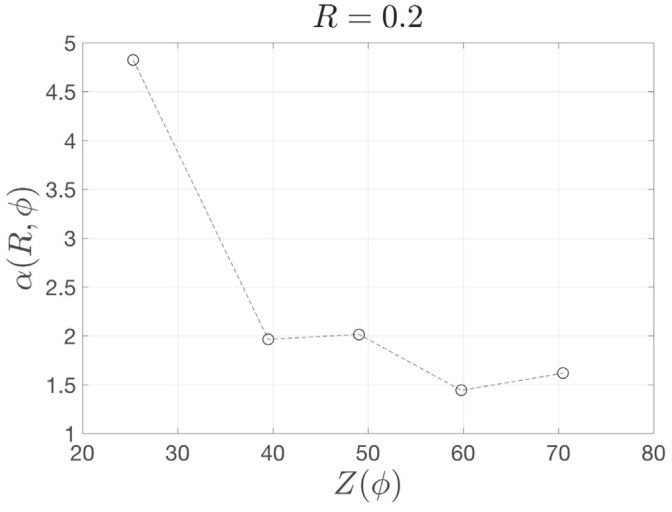

Fig. 8. Exponent of HS Eq. (54) with respect to the brittleness number $Z(\phi)$ at $R = 0.2$.

Data availability

The raw data required to reproduce these findings are available to download from
https://doi.org/10.13140/RG.2.2.35945.19046
The processed data required to reproduce these findings are available to download from
https://doi.org/10.13140/RG.2.2.35945.19046

Acknowledgments

The author would like to acknowledge Rolls-Royce plc for their support of this research through the Composites University Technology Centre at the University of Bristol (UK).

Appendix A. Normalised elastic constants

The normalised elastic constants for a two-dimensional plane stress regime are given by [42,44]

$$\lambda = \frac{E_3}{E_1}, \quad \rho = \sqrt{\frac{E_3}{E_1}}\left(\frac{E_1}{2G_{13}} - \nu_{13}\right). \tag{A.1}$$

The material constants that appear in the relation between the ERR and SIF components in Eq. (1) are expressed as follows [42,44]:

$$\alpha_I = \sqrt[4]{\lambda}\sqrt{\frac{1}{E_1}\frac{1}{E_3}\frac{1+\rho}{2}}, \quad \alpha_{II} = \frac{1}{\sqrt[4]{\lambda}}\sqrt{\frac{1}{E_1}\frac{1}{E_3}\frac{1+\rho}{2}}. \tag{A.2}$$

Appendix B. Supplementary data

Supplementary data to this article can be found online at https://doi.org/10.1016/j.matdes.2018.05.049.

References

[1] G. Allegri, M.I. Jones, M.R. Wisnom, S.R. Hallett, A new semi-empirical model for stress ratio effect on mode II fatigue delamination growth, Compos. Part A 42 (7) (2011) 733–740.
[2] G. Allegri, M.R. Wisnom, A non-linear damage evolution model for mode II fatigue delamination onset and growth, Int. J. Fatigue 43 (2012) 226–234.
[3] G. Allegri, M.R. Wisnom, S.R. Hallett, A new semi-empirical law for variable stress-ratio and mixed-mode fatigue delamination growth, Compos. Part A 48 (2013) 192–200.
[4] J. Andersons, M. Hojo, S. Ochiai, Model of delamination in brittle-matrix composites under cyclic loading, J. Reinf. Plastic Compos. 20 (5) (2001) 431–450.
[5] J. Andersons, M. Hojo, S. Ochiai, Empirical model for stress ratio effect on fatigue delamination growth rate in composite laminates, Int. J. Fatigue 26 (6) (2004) 597–604.
[6] F. Aymerich, M. Serra, Prediction of fatigue strength of composite laminates by means of neural networks, Key Eng. Mat. 144 (1998) 231–240.
[7] A.A. Baker, R. Jones, R.J. Callinan, Damage tolerance of graphite/epoxy composites, Compos. Struct. 4 (1) (1985) 15–44.
[8] G.I. Barenblatt, Y. a. B. Zeldovich, Intermediate asymptotics in mathematical phyisics, Russ. Math. Surv. 26 (1971) 45–61.
[9] G.I. Barenblatt, L.R. Botvina, Incomplete self-similarity of fatigue in the linear range of crack growth, Fat. Fract. Engng. Mat. Struct. (FFEMS) 3 (1981) 193–212.
[10] G.I. Barenblatt, L.R. Botvina, A note concerning power-type constitutive equations of deformation and fracture of solids, Int. J. Eng. Sci. 20 (2) (1982) 187–191.
[11] G.I. Barenblatt, S.-S. Scaling, I. Asymptotics, Self-similarity and Intermediate Asymptotics, Cambridge University Press, Cambridge, UK, 1996.
[12] G.I. Barenblatt, Scaling phenomena in fatigue and fracture, Int. J. Fract. 138 (2006) 19.
[13] A.J. Brunner, S. Stelzer, A. Mujtaba, R. Jones, Examining the application of the Hartman-Schijve equation to the analyisis of cyclic fatigue fracture of polymer-matrix composites, Theor. App. Fract. Mech. 92 (2017) 420–425.
[14] E. Buckingham, On physically similar systems: illustrations of the use of dimensional equations, Phys. Rev. 4 (4) (1914) 345–376.
[15] A. Carpinteri, Stability of fracturing process in RC beams, J. Struct. Eng. 110 (3) (1984) 544–558.
[16] A. Carpinteri, Scaling laws and renormalization for strength and toughness of disordered materials, Int. J. Solids Struct. 31 (1994) 291–302.
[17] I. Chou, I. Kimpara, K. Kageyama, I. Ohsawa, Mode I and mode II fracture toughness measured between differently oriented plies in graphite epoxy composites, Composite Materials: Fatigue and Fracture (Fifth Volume); ASTM STP, 1230, 1995, pp. 132–151.
[18] M. Ciavarella, M. Paggi, A. Carpinteri, One, no one and one hundred thousands crack propagation laws: a generalised Barenblatt and Botvina dimensional analysis approach to fatigue crack growth, J. Mech. Phys. Solids 56 (12) (2008) 3416–3432.
[19] H. El Kadi, Y. Al-Assaf, Prediction of the fatigue life of unidirectional glass fiber/epoxy composite laminate using different neural network paradigms, Compos. Struct.; addto contour55 (2002) 239–246.
[20] N. Goldenfeld, O. Martin, Y. Oono, Intermediate asymptotics and renormalization group theory, J. Scientific Computing 4 (4) (1989) 355–372.
[21] E.S. Greenhalgh, Failure Analysis and Fractography of Polymer Composites Chapter, 5. Woodhead Publishing Limited, Cambridge, UK, 2009.
[22] A. Hartman, J. Schijve, The effects of environment and load frequency on the crack propagation law for macro fatigue crack growth in aluminium alloys, Eng. Fract. Mech. 1 (4) (1970) 615–631.
[23] M. Hojo, K. Tanaka, C.G. Gustafson, R. Hayashi, Effect of the stress ratio on near-threshold propagation of delamination fatigue cracks in unidirectional CFRP, Compos. Sci. Tech. 29 (1987) 273–292.
[24] M. Hojo, S. Ochiai, C.G. Gustafson, K. Tanaka, Effect of matrix resin on delamination fatigue crack growth in CFRP laminates, Eng. Fract. Mech. 49 (1) (1994) 35–47.
[25] G. Huang, Q. Zhu, C. Siew, Extreme learning machine: theory and applications, Neurocomputing 70 (2006) 489–501.
[26] G. Huang, D.H. Wang, Y. Lan, Extreme learning machines: a survey, Int. J. Mach. Learn. Cyber. 2 (2011) 107–122.
[27] W.G. Jiang, S. Hallett, B. Green, M. Wisnom, A concise interface constitutive law for analysis of delamination and splitting in composite materials and its application to scaled notched tensile specimens, Int. J. Numer. Meth. Eng. 69 (2007) 1982–1995.
[28] R. Jones, S. Pitt, A.J. Brunner, D. Hui, Application of the Hartman-Schijve equation to represent mode I and mode II fatigue delamination growth in composites, Compos. Struct. 94 (2012) 1343–1351.
[29] R. Jones, Fatigue crack growth and damage tolerance, Fract. Engng. Mat. Struct. (FFEMS) 37 (5) (2014) 463–483.
[30] R. Khan, R. Alderliesten, L. Yao, R. Benedictus, Crack closure and fibre bridging during delamination growth in carbon fibre/epoxy laminates under mode I fatigue loading, Compos. Part A 67 (2014) 201–211.
[31] R. Khan, R. Alderliesten, S. Badshah, R. Benedictus, Effect of stress ratio or mean stress on fatigue delamination growth in composites: critical review, Compos. Struct. 124 (2015) 214–227.
[32] J.A. Lee, D.P. Almond, B. Harris, The use of neural networks for the prediction of fatigue lives of composite materials, Compos. A 30 (10) (1999) 1159–1169.
[33] J.F. Mandell, U. Meier, Fatigue crack propagation in 0°/90° E-glass/epoxy composites, ASTM STP 569 (1975) 28–44.
[34] G. Murri, Evaluation of Delamination Onset and Growth Characterization Methods Under Mode I Fatigue Loading, National Aeronautics and Space Administration Technical Memorandum; NASA/TM-2013-0010557, 2013.
[35] T.K. O'Brien, Characterization of delamination onset and growth in a composite laminate, Damage in Composite Materials; ASTM STP, 775, 1982, pp. 140–167.
[36] Toland, T.K. O'Brien, W.M. Johnston, Mode II Interlaminar Fracture Toughness and Fatigue Characterization of a Graphite Epoxy Composite Material, National Aeronautics and Space Administration Technical Memorandum; NASA/TM-2010-216838, 2010.
[37] C. Rans, R. Alderliesten, R. Benedictus, Misinterpreting the results: how similitude can improve our understanding of fatigue delamination growth, Compos. Sci. Tech. 71 (2) (2011) 230–238.
[38] J.G. Ratcliffe, J.M. Johnston, Jr, Influence of mixed mode I-mode II loading on fatigue delamination growth characteristics of a graphite epoxy tape laminate, 29th ASC Technical Conference, San Diego, CA. 2014,
[39] R.O. Ritchie, Incomplete self similarity and fatigue crack growth, Int. J. Fract. 132 (2005) 197–203.
[40] R.O. Ritchie, Mechanisms of fatigue crack propagation in metals, ceramics and composites: role of crack tip shielding, Mat. Sci. Eng. 103 (1) (1988) 15–28.
[41] J. Rouchon, Fatigue and damage tolerance evaluation of structures: the composite materials response, NLR-TP-2009-221, 2009.
[42] G.C. Sih, P.C. Paris, G.R. Irwin, On cracks in rectilinearly anisotropic bodies, Int. J Fracture Mech. 1 (1965) 189–203.
[43] A. Spagnoli, Self-similarity and fractals in the Paris range of fatigue crack growth, Mech Mater. 37 (2005) 519–529.
[44] Z. Suo, G. Bao, B. Fan, T.C. Wang, Orthotropy rescaling and implication for fracture in composites, Int. J. Solids Struct. 28 (2) (1991) 235–248.
[45] K. Tanaka, H. Tanaka, T. Tsuji, K. Yamagishi, Effect of stress ratio on mode I propagation of interlaminar fatigue cracks in CFRP, J. Soc. Mat. Sci. Jpn. 44 (502) (1995) 960–966.
[46] K. Tanaka, H. Tanaka, Stress ratio effect on mode II propagation of interlaminar fatigue cracks in graphite/epoxy composites, Composite Materials: Fatigue and Fracture (Sixth Volume); ASTM STP, 1285, 1997, pp. 126–142.
[47] H. Tanaka, K. Tanaka, T. Tsuji, H. Katoh, Mixed-mode (I + II) propagation of delamination fatigue cracks in unidirectional graphite/epoxy laminates, Trans. Jpn. Soc. Mech. Eng. A 65 (636) (1999) 1676–1683.
[48] J. Tomblin, W. Seneviratne, Determining the Fatigue Life of Composite Aircraft Structures Using Life and Load-Enhancement Factors, DOT/FAA/AR-10/6, 2011.
[49] L. Yao, R. Alderliesten, R. Jones, A.J. Kinloch, Delamination fatigue growth in polymer-matrix fibre composites: a methodology for determining the design and lifing allowables, Compos. Struct. 196 (2018) 8–20.
[50] H. Zhu, E.C.C. Tsang, X.Z. Wang, R.A.R. Ashfaq, Monotonic classification extreme learning machine, Neurocomputing 225 (2017) 205–213.